NTNU

Norwegian University of Science and Technology

Department of Materials Science and Engineering

TMT4208 Strømning og varmeoverføring, Videregående kurs

Investigation of flow and heat transfer conditions using CFD

Author
Candidate 11

Subject manager
Kristian E. Einarsrud

April 12, 2021

Contents

1 Introduction

In this report flow conditions in a closed cavity with one moving wall, heat transport from a heated cylinder to a working fluid and bubble behaviour are studied by CFD using OpenFOAM, visualized using ParaView. OpenFOAM is an open source implementation of several finite volume methods. These methods rely on discretizing the simulated volume by a process called *meshing*. Having an adequate mesh resolution is necessary if physically sound results are to be acquired. However, required computational time can increase rapidly with mesh resolution. When computational resources are limited, a trade off must be made between computational efficiency and result accuracy.

When the volume to be simulated has been discretized one of several methods can be chosen to solve the Navier-Stokes, continuity and if necessary energy conservation equations, numerically at each node. Due to the finite volume method requiring a volume, not an area, two dimensional simulations are run as three dimensional simulations with a single volume element in thickness.

For simulations run in this report a MacBook Pro running Windows 10 with a 4 core 2.5 GHz intel i5 CPU (Turbo Boost to 3.1 GHz) with 3 MB L3 Cache and 10 GB 1866 MHz DDR3 memory has been used. OpenFOAM was run through the SimFlow UI, note that the version of SimFlow used only allows for two CPU cores to be utilized for solving and one core for meshing.

2 Circulation in a cavity

In this section, steady state circulation in a cavity with one moving wall is investigated. First, a mesh convergence study is conducted using the baffle geometry shown in Figure 2.1b with a wall velocity of $u_{\text{wall}} = 0.1\,\text{m}\,\text{s}^{-1}$, increasing the resolution until the computed viscous force on the leftmost wall in the y-direction converges. Then, the effect of varying the velocity of the moving wall in the geometry shown in Figure 2.1a is investigated, before the effect of introducing a corner and a baffle as shown in Figures 2.1c and 2.1b respectively are analysed. Finally the shear force on the leftmost wall is compared for the three geometries at constant velocity. The required computation time for all cases investigated are displayed in Table 2.1.

For all computations the SimpleFOAM solver is used, this is a steady state incompressible solver. For pressure the GAMG solver was used, for velocity the PBiCG Stabilized solver was used. For the corner geometry, the effect of changing the gradient scheme from "Gauss Linear" to fourth order least squares was investigated.

2.1 Mesh convergence

An equipartitioned mesh with an increasing number of cells was used to compute the steady state flow conditions for the geometry shown in Figure 2.1b with a moving wall velocity of $u_0 = 0.1\,\text{m}\,\text{s}^{-1}$. For all resolutions, a boundary layer mesh around the baffle consisting of five layers, with an expansion ratio of 1.25 and a first layer thickness of 0.2 was used. The viscous force in the y-direction on the leftmost wall was chosen as the parameter

Table 2.1: Computation times for simulations of flow in a cavity. Remaining times for simulations run in the mesh convergence study are found in Table A.1. Geometries are shown in Figure 2.1. *Using the numerical settings described in section 2.3.1.

Geometry	Wall velocity [$\mathrm{m\,s^{-1}}$]	Mesh [cells x cells]	Clock time [s]
Plain	0.01	195x195	278
Plain	0.1	195x195	183
Plain	1	195x195	437
Baffle	0.1	15x15	2
Baffle	0.1	50x50	7
Baffle	0.1	115x115	31
Baffle	0.1	195x195	192
Corner	0.1	195x195	1316
Corner	0.1	195x195	1380*

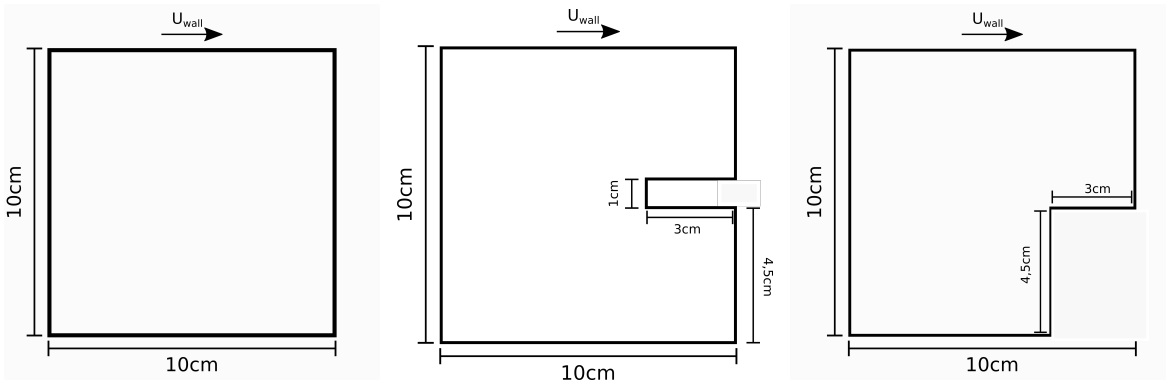

(a) Plain Geometry (b) Baffle Geometry (c) Corner Geometry

Figure 2.1: Geometries investigated in Section 2. Upper wall uses moving wall velocity, zero pressure gradient boundary conditions, remaining walls use no slip, zero pressure gradient boundary conditions.

to determine mesh convergence. The flow fields displayed in Figure 2.3 show that an increasing number of vortices were resolved with increasing resolution. Additionally, the magnitude of the velocity changed as more vortices were resolved. Further increasing the resolution beyond 195x195 cells did not notably change the flow conditions.

The existence of these vortices effects the computed shear stress on the leftmost wall, and as shown in Figure 2.2, the shear stress did not converge until a resolution of 195x195 cells was used. Following this result, a mesh of 195x195 cells was used for all computations in this section. Computations on the geometry shown in Figure 2.1c also use a boundary layer mesh around the corner consisting of five layers, with an expansion ratio of 1.25 and a first layer thickness of 0.2.

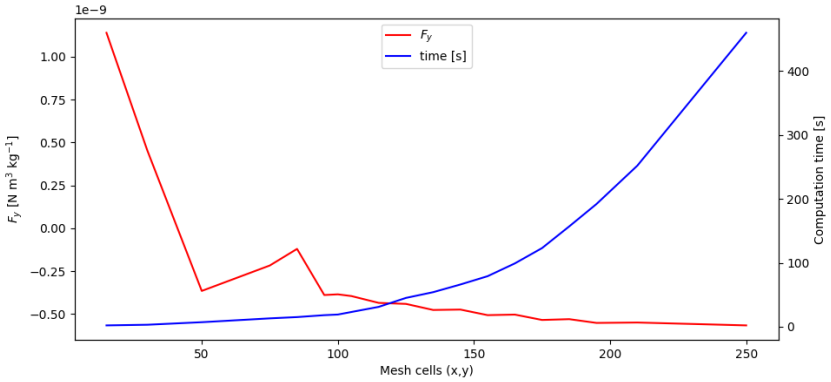

Figure 2.2: Convergence of y-component of viscous force on leftmost wall and increase in computation time with increasing resolution.

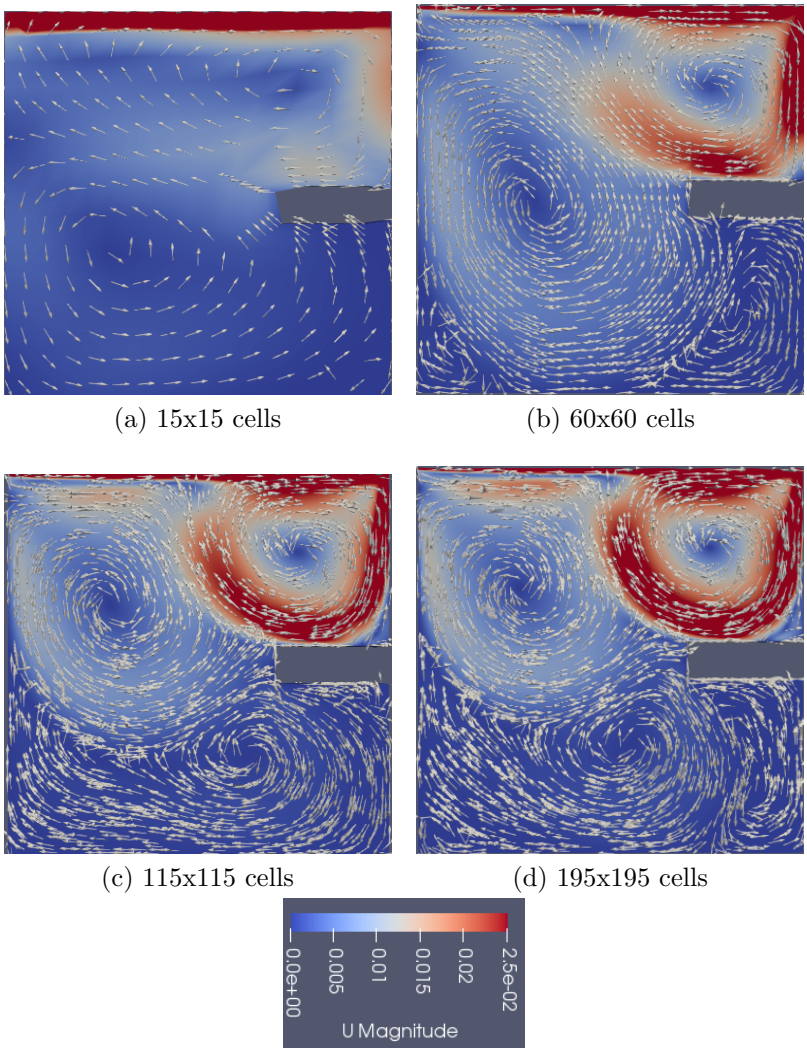

(a) 15x15 cells

(b) 60x60 cells

(c) 115x115 cells

(d) 195x195 cells

Figure 2.3: An increasing number of vortices were resolved as the resolution was increased. Additionally, the magnitude of the velocity changed notably in several areas.

2.2 Varying wall velocities

The flow conditions at an upper wall velocity of $0.01\,\mathrm{m\,s^{-1}}$, $0.1\,\mathrm{m\,s^{-1}}$ and $1\,\mathrm{m\,s^{-1}}$ were investigated for the geometry shown in Figure 2.1a, using a mesh as described in section 2.1. The velocity fields shown in Figure 2.4 shows that an increasing wall velocity leads to increased size of the central vortex. At the same time, the velocity of the circulating fluid relative to the velocity of the wall decreases with increasing wall velocity.

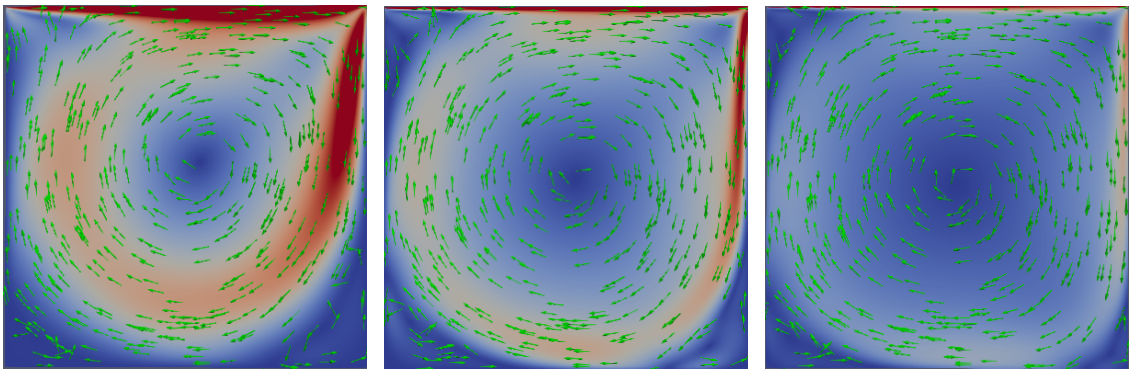

(a) $u_{wall} = 0.01\,\mathrm{m\,s^{-1}}$ (b) $u_{wall} = 0.1\,\mathrm{m\,s^{-1}}$ (c) $u_{wall} = 1\,\mathrm{m\,s^{-1}}$

Figure 2.4: Flow conditions in a cavity with varying upper wall velocity. Colormap indicates |u| with linear scaling from dark red indicating $|\mathrm{u}| \geq \frac{1}{2}u_{wall}$ to white indicating $|\mathrm{u}| = \frac{1}{4}u_{wall}$ to dark blue indicating $|\mathrm{u}| = 0$.

Closer comparison of the velocity profiles along the horizontal and vertical line that intersect at the center of the cavity is shown in Figure 2.5 clearly show that the central vortex moves off-center as the velocity is reduced. It is also noted that maximum relative velocity in the y-direction, computed as $(\frac{v}{|v_{min}|})$ is close to constant and equal to $\approx -0.6v_{min}$ for all wall velocities, while the minimum relative velocity in the x-direction $(\frac{u}{v_{max}})$ changes notably. This means that while velocity close to the leftmost wall scales linearly with velocity close to the rightmost wall, the same is not the case for the top and bottom walls.

2.3 Baffle and corner

The most evident changes in flow conditions resulting from the addition of a baffle and a corner are that the flow along the rightmost wall is deflected, reversing the direction of the vortex close to the leftmost wall, as seen in Figure 2.6. Additionally, in the case of the baffle geometry, the fluid in the lower half of the cavity is close to still, as seen from Figures 2.6b and 2.7b.

Introducing a corner gives the same effect as a baffle in the upper half of the cavity, with equal directions and similar magnitudes, as shown in Figure 2.7. In the lower half of the cavity, a completely different effect is observed. The corner deflects the flow along the bottom wall, preventing the formation of a third vortex, thereby causing the fluid at the bottom wall to flow in the opposite direction of that in the baffle geometry. Additionally, the flow in the bottom half of the cavity has a higher velocity.

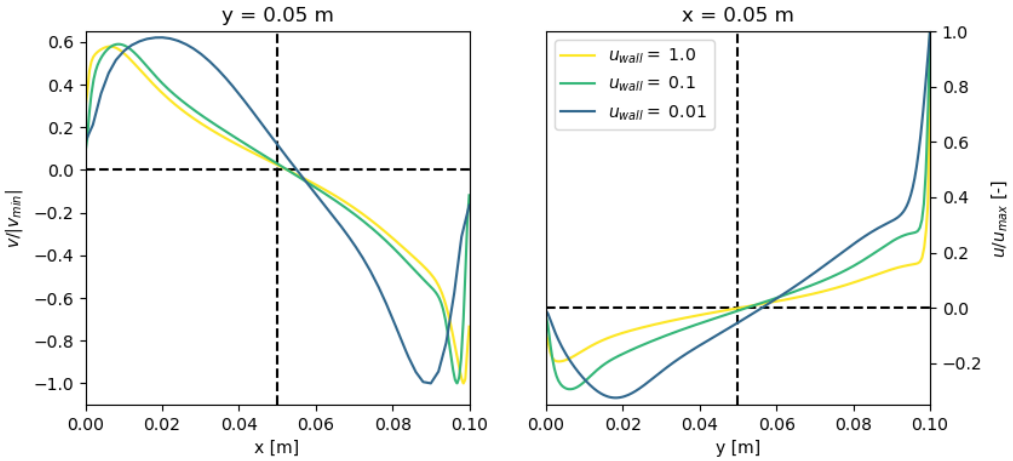

Figure 2.5: Left) Relative velocity in the y-direction along the horizontal line at y = 0.05 m. Right) Relative velocity in the x-direction along the vertical line at x = 0.05 m.

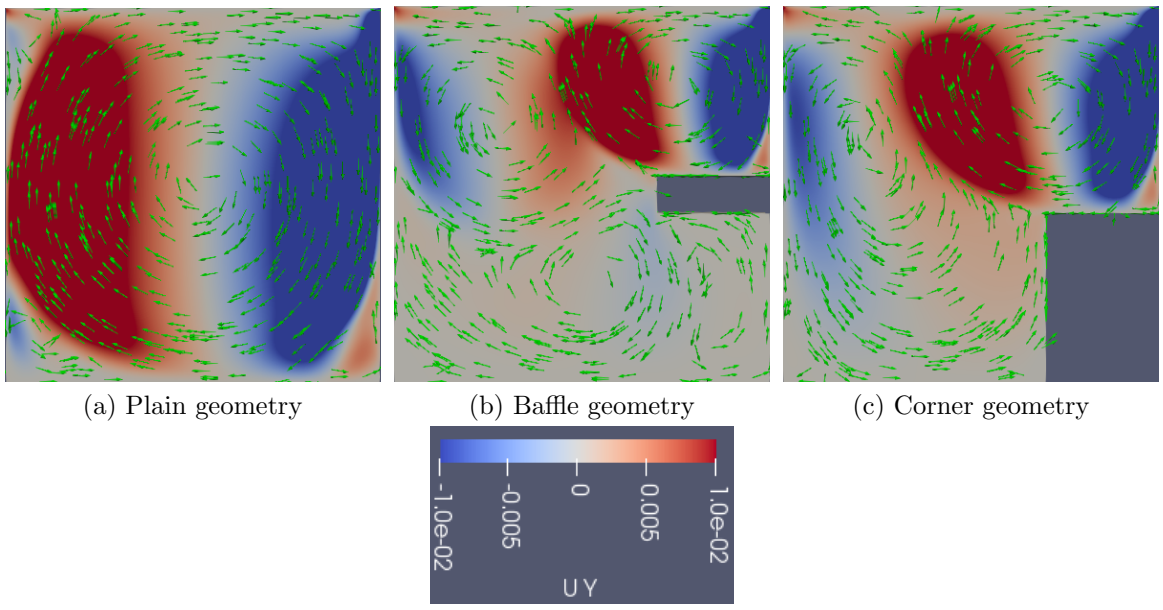

(a) Plain geometry (b) Baffle geometry (c) Corner geometry

Figure 2.6: Comparrison of the flow fields in the three geometries with a top wall velocity of 0.1 m s^{-1}. Color map illustrates velocity y-components in m s^{-1}.

2.3.1 Changing numerical scheme

Changing the gradient scheme from Gauss linear to fourth order least squares did not visually change the resulting flow. A plot of the velocity profile close to the leftmost wall was also indistinguishable from the result shown in Figure 2.8. However, as shown in Table 2.2 the computed viscous force and resulting shear stress on the leftmost wall changes significantly. This is due to the force on the wall being dependent on the velocity gradient close to the wall. As the "Gauss linear" scheme is a second order scheme that requires interpolation from nodes to cell centers, while the fourth order least squares scheme is a fourth order scheme,[1] the result obtained using the latter may be more

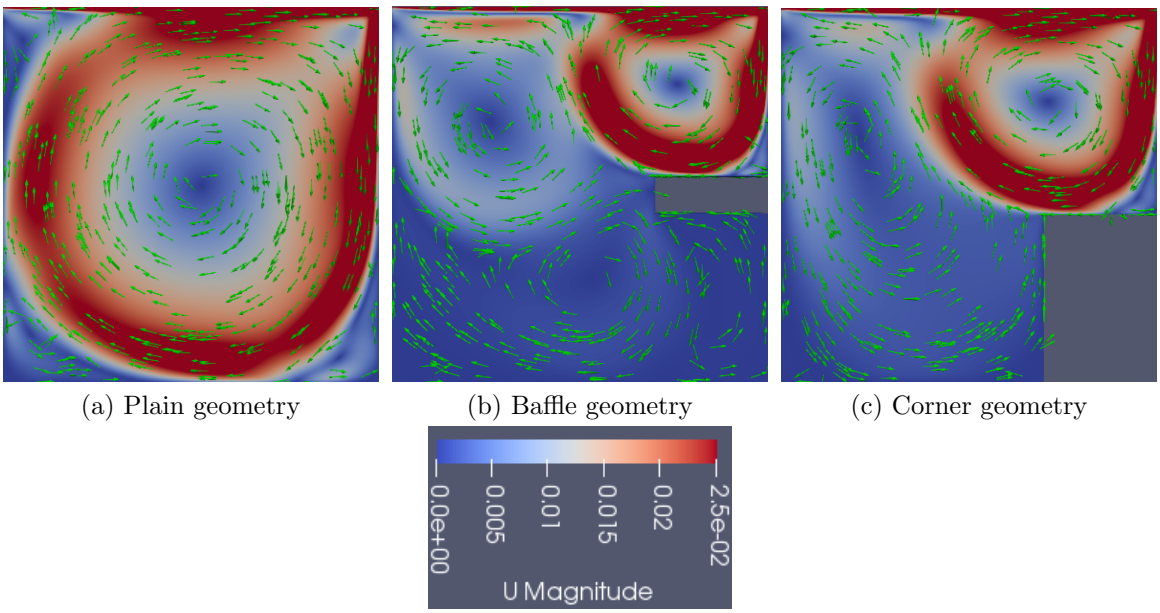

(a) Plain geometry (b) Baffle geometry (c) Corner geometry

Figure 2.7: Comparrison of the flow fields in the three geometries with a top wall velocity of $0.1\,\mathrm{m\,s^{-1}}$. Colormap illustrates velocity magnitude in $\mathrm{m\,s^{-1}}$.

precise. As seen from Table 2.1 the increase in required computational time was very small, and may very well be the result of other factors than the change in numerical settings (other processes being run during the computation etc.).

2.3.2 Shear forces

The shear force on the leftmost wall of the cavity was compared for the three geometries by comparing the y-component of the viscous force on the wall, which can be directly monitored in SimFlow. The SimpleFOAM incompressible solver uses kinematic pressure in its calculations,[1] therefore returned force values must be multiplied by the density of the fluid to acquire values in Newtons. Further, because OpenFOAM uses finite volume methods in its calculations the mesh has a finite depth, despite the formulated problem being two dimensional. In this case the extruded mesh has a depth of $0.01\,\mathrm{m}$, giving the leftmost wall an area of $0.001\,\mathrm{m^2}$. Finally, the shear stress on the wall can be computed as $\tau = \frac{F_y \rho}{A}$ where F_y is the force in the y-direction returned in SimFlow, ρ is the density of water and A is the area of the leftmost wall.

The computed shear stresses are displayed in Table 2.2. The first thing to note is that the plain geometry has a positive shear stress, the force on the wall is acting in the positive y-direction. The corner and baffle geometries on the other hand have negative shear stresses on the leftmost wall. This is due to the corner and baffle deflecting the flow along the rightmost wall forming a vortex with opposite rotational direction to the central vortex in the plain geometry, as shown in Figure 2.6. The sign of the shear stresses coincide with the primary direction of the flow close to the wall, as displayed in Figure 2.8.

Table 2.2: Computed shear stress on the leftmost wall for different geometries, with a top wall velocity of $0.1\,\mathrm{m\,s^{-1}}$. *Using numerical settings described in section 2.3.1.

Geometry	Plain	Corner	Baffle	Corner*
Shear stress [mPa]	4.51	-0.352	-0.551	-0.077

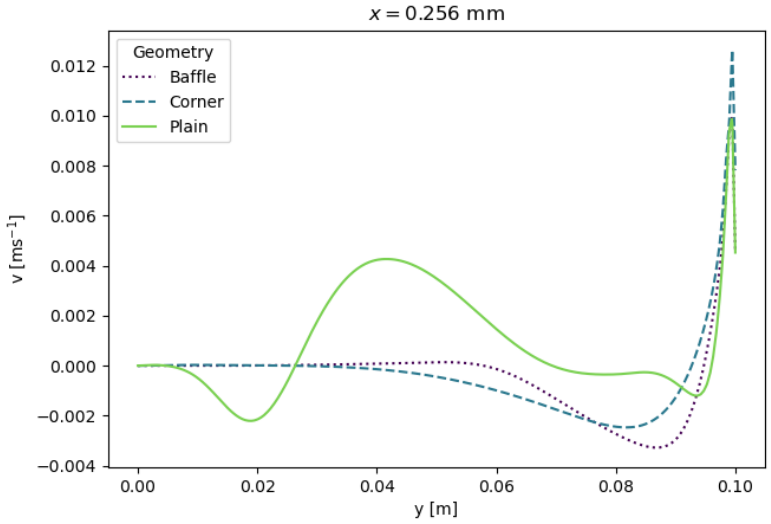

Figure 2.8: y-component of velocity at one half mesh cell away from the leftmost wall, for different geometries.

3 Flow around a heated cylinder

In this section fluid flow around a heated cylinder, with geometry as shown in Figure 3.1 is investigated. Firstly a mesh convergence study is conducted to determine the mesh to be used in the simulations, then the effect of varying inlet velocity on the flow conditions and heat transfer is investigated. Lastly, the effect of changing the working fluid from water to air is looked upon. Computation times for the various cases are reported in Table 3.1, the complete set of computation times from the mesh convergence study are reported in Table A.2.

The BouyantPIMPLE solver was used with the implicit Euler scheme for time discretisation and second order Gaussian integration (i.e. "Gauss linear") as the gradient scheme. The time stepping was set to automatic with an initial time step of 0.2 s, maximum time step of 0.5 s and a maximum Courant number of 1. The effect of changing the time discretisation scheme from the implicit Euler method to the Crank-Nicholson method (pure Crank-Nicholson, without corrections using Euler) was tested when using water with an inlet velocity of $0.015\,\mathrm{m\,s^{-1}}$ as the working fluid.

3.1 Mesh convergence

The required resolution of the mesh was determined by computing the steady state heat transfer from the cylinder to the fluid at an inlet velocity of $u_0 = 0.01\,\mathrm{m\,s^{-1}}$ as described in

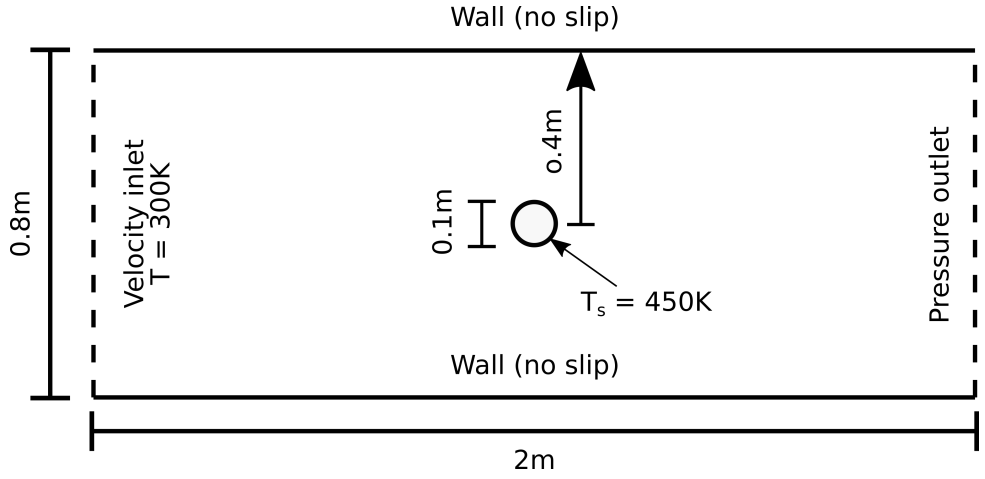

Figure 3.1: Geometry and boundary conditions investigated in section 3.

Table 3.1: Computation times for simulation of flow around a heated cylinder. Velocity refers to inlet velocity. All simulations use 100x100 mesh, with a 3/1.25/0.5 (Nr. layers/-expantion factor/initial layer thickness) boundary layer mesh around the cylinder, and a refined mesh with two levels of refinement extending 5 cm from the cylinder. *Using the Crank-Nicholson time discretisation scheme.

Inlet Velocity [$\mathrm{m\,s^{-1}}$]	Working Fluid	Time simulated [s]	Clock time [s]
0.01	Water	1000	492
0.015	Water	500	586
0.005	Water	2500	2361
0.005	Air	750	1085
0.015	Water	500	842*

section 3.5 at varying mesh resolution. The heat transfer is expected to depend upon the behaviour of the thermal boundary layer δ_T^*, which in turn depends on the momentum film thickness δ^*. To acquire an idea of the order of magnitude involved, the thermal boundary layer thickness was estimated as

$$\delta_T^* = \delta^* \mathrm{Pr}^{-\frac{1}{3}} = 3.01 \mathrm{Pr}^{-\frac{1}{3}} \sqrt{\frac{\nu d}{u_\infty}} \tag{3.1}$$

where d is the cylinder diameter and u_∞ is the inlet velocity. This gives $\delta_T^* \approx 5\,\mathrm{mm}$. This implies that the mesh cells near the cylinder should have dimensions $<< 5\,\mathrm{mm}$, therefore a boundary layer mesh was used, as it is not viable, and likely not necessary, to mesh the entire geometry with this resolution. The boundary layer mesh was also varied, and will in this section be reported as (number of layers/expansion factor/initial layer thickness).

As shown in Figure 3.2 the computed steady state heat transfer changes only marginally when increasing the mesh resolution beyond 100x100 cells, using a boundary layer mesh (5/1.25/0.2). At this resolution, changing the boundary layer mesh to (10/1.1/0.2) resulted in small changes in the development of the heat flux in time, but did not no-

tably change the steady state heat flux. Further increasing the boundary layer mesh to (15/1.1/0.05) significantly changed the steady state heat flux, but upon visual inspection the mesh was unable to properly resolve the transition from the boundary layer to the high temperature "tails" trailing behind the cylinder. Adding a refined mesh with two levels of refinement extending 5 cm away from the cylinder, and reducing the boundary layer mesh to (3/1.25/0.5) allowed resolution of this transition, as well as the thermal boundary layer. As the thermal boundary layer is of interest in this section, this mesh was chosen for the remaining calculations. Note that despite having higher (relative) initial layer thickness, the (3/1.25/0.5) boundary layer mesh within the refined mesh has a higher resolution at the boundary layer than the (15/1.1/0.05) boundary layer mesh without the refined geometry, due to the initial layer thickness being relative to the mesh that surrounds the boundary layer.

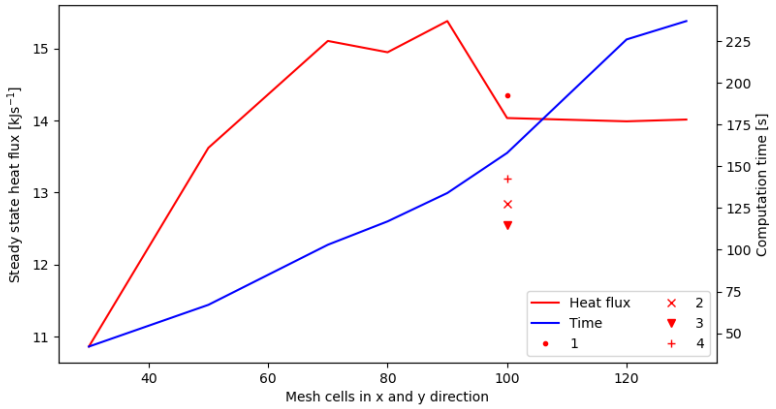

Figure 3.2: Mesh convergence study at inlet velocity $u_0 = 0.01\,\mathrm{m\,s^{-1}}$. Line indicates heat fluxes calculated with a (5/1.25/0.2) boundary layer mesh. Marks are heat fluxes computed with boundary layer meshes 1: 10/1.1/0.2, 2: 15/1.1/0.1, 3: 15/1.2/0.05, 4: 3/1.25/0.5. 4 also used a refined mesh with two levels of refinement extending 5 cm away from the cylinder.

3.2 Varying velocities

The flow and heat transfer conditions were investigated with inlet velocities of $0.005\,\mathrm{m\,s^{-1}}$, $0.01\,\mathrm{m\,s^{-1}}$ and $0.015\,\mathrm{m\,s^{-1}}$. These velocities were chosen to ensure laminar conditions, as calculation of the Reynolds number shows that

$$\begin{aligned} Re_d = \frac{\rho U_{inlet} d}{\mu} &< 2000 \\ U_{inlet} &< \frac{2000\mu}{\rho d} \approx 0.02\,\mathrm{m\,s^{-1}} \end{aligned} \tag{3.2}$$

As shown in Figure 3.3 the heat transfer conditions are qualitatively similar for the three cases when the flow reaches a quasi-steady state, however the time required to reach quasi-steady state increases rapidly with decreasing inlet velocity. The most notable difference in the temperature field is that the high temperature region directly behind the cylinder

grows in size with decreasing inlet velocity, resulting in a higher temperature at the outlet. This is discussed further in section 3.5. The velocity profiles shown in Figures 3.4a-c show that the velocity fields are also qualitatively similar in the quasi-steady state.

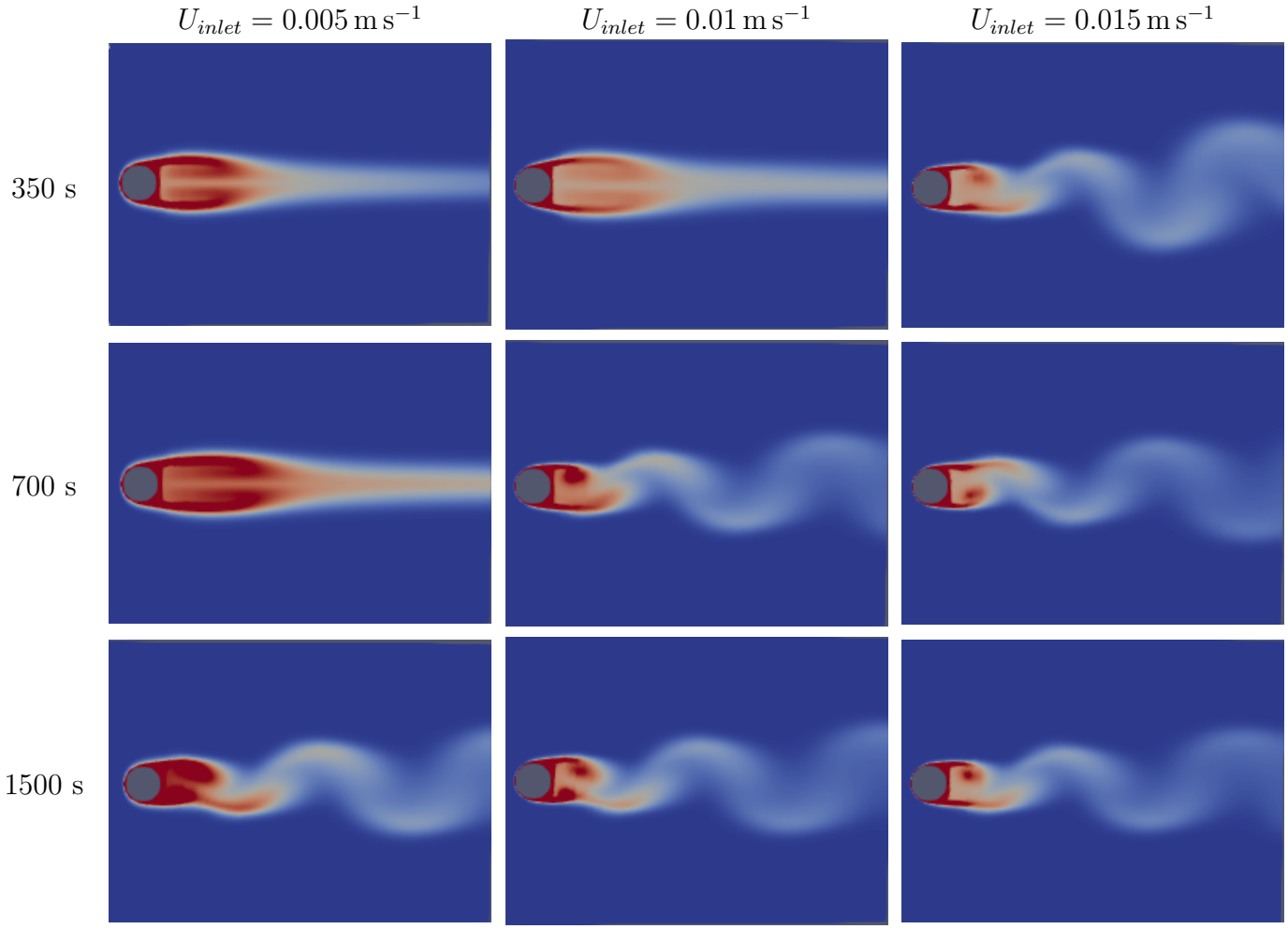

Figure 3.3: Development of temperature profile with time at different inlet velocities. Colormap indicates temperature ranging linearly from red: 310 K to blue: 300 K.

The primary differences at steady state between the cases with different inlet velocities are the temperature and velocity gradients directly behind the heated cylinder. The relative velocity $\frac{|u|}{u_{inlet}}$, shown for an inlet velocity $0.005\,\mathrm{m\,s^{-1}}$ in Figure 3.4d, is virtually indistinguishable for the three inlet velocities. This implies that the velocity and velocity gradient in each point scales close to linearly with the inlet velocity.

3.3 Changing numerical settings

Changing the time discretisation scheme from implicit Euler to Crank-Nicholson did not visually change the results when water with an inlet velocity of $0.015\,\mathrm{m\,s^{-1}}$ was used. The Crank-Nicholson method is a linear combination of the implicit and explicit Euler methods and is unconditionally stable.[2] The implicit Euler method is also stable, but the Crank-Nicholson method has a higher order of accuracy in time than the implicit Euler

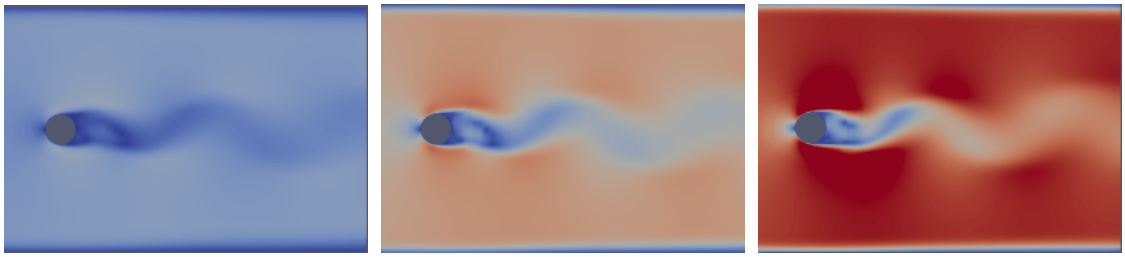

(a) $u_{inlet} = 0.005\,\mathrm{m\,s^{-1}}$ (b) $u_{inlet} = 0.01\,\mathrm{m\,s^{-1}}$ (c) $u_{inlet} = 0.015\,\mathrm{m\,s^{-1}}$

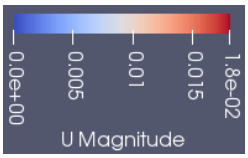

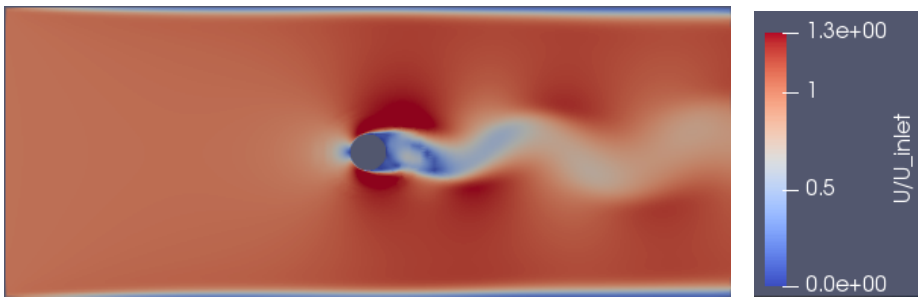

(d) Relative velocity, $u_{inlet} = 0.005$

Figure 3.4: a-c) Velocity profiles at different inlet velocities, at time a) 2500 s, b) 1000 s, c) 500 s. d) Velocity relative to inlet velocity, with inlet velocity $0.005\,\mathrm{m\,s^{-1}}$. The relative velocity profiles are indistinguishable for different inlet velocities.

method. The fact that oscillations in the wake of the cylinder were indistinguishable when using the Crank-Nicholson method and the implicit Euler method indicates that they are not the result of numerical inaccuracy or instability, but rather a true physical phenomena.

3.4 Air as working fluid

The simulation was run with an inlet velocity of $0.005\,\mathrm{m\,s^{-1}}$ and air as the working fluid. The major difference of importance between air and water in this simulation is the difference in kinematic viscosity. Air has a kinematic viscosity about one order of magnitude larger, leading to a lower Reynolds number and a far higher momentum film thickness and thicker thermal boundary layer. This, combined with the low heat capacity and conductivity of air lead to a greatly reduced heat transport from the cylinder to the fluid, as shown in Table 3.9.

The flow around the cylinder also changes qualitatively with the change in working fluid, as shown in Figure 3.5. The low pressure region that forms behind the cylinder when using water as the working fluid, which eventually causes the "tail" behind the cylinder to oscillate does not form when using air as the working fluid, as shown in Figure 3.6.

The fact that the low pressure region seen when using water as the working fluid does not

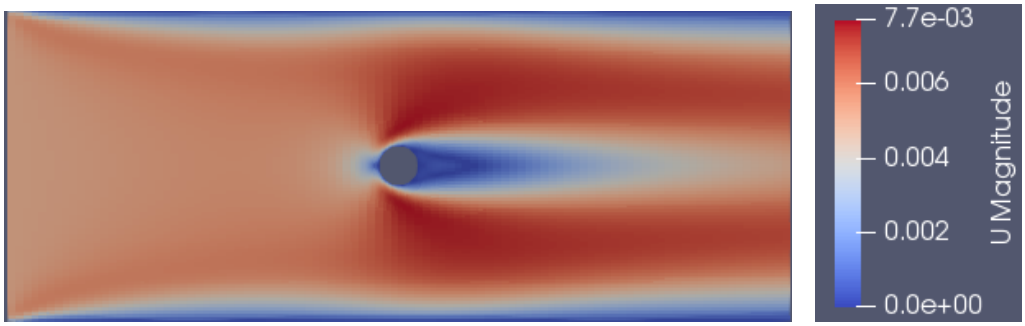

Figure 3.5: Velocity field of air flow around cylinder with inlet velocity $0.005\,\mathrm{m\,s^{-1}}$, after 300 s.

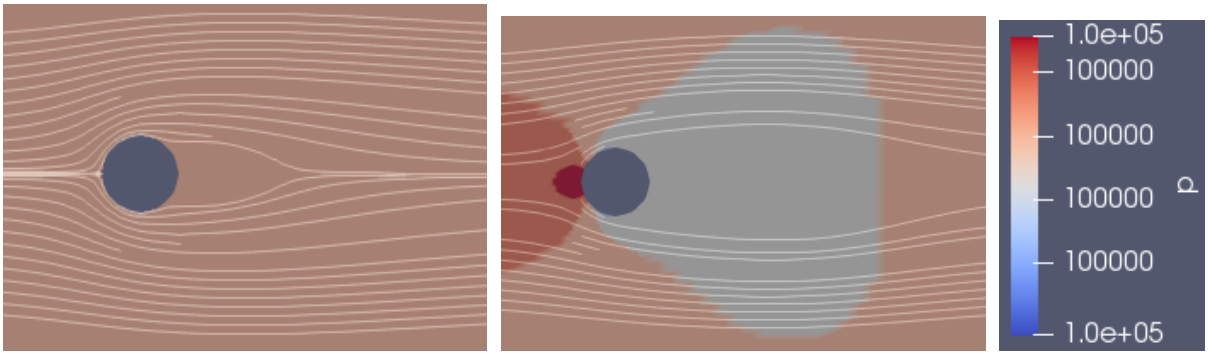

(a) Air (b) Water

Figure 3.6: Pressure and streamlines when using a) Air, and b) Water, as working fluid after 750 s. Inlet velocity in both cases is $0.005\,\mathrm{m\,s^{-1}}$.

form when air is used also explains the large difference in the development of heat flux and average outlet temperature seen in Figure 3.9. The spike in temperature and heat flux seen before the quasi-steady state is reached does not appear when using air. This spike coincides with the time at which the low pressure region behind the cylinder grows large enough to destabilize the "tail", at this time heat that has accumulated in that region is transported to the outlet as the "tail" begins to oscillate, as shown in Figure 3.7.

3.5 Heat transfer

The heat transfer from the cylinder to the fluid was analyzed by calculating the heat flux out of the simulated control volume. Due to the simulation being run as a 2D case, heat flux is reported in $\mathrm{W\,m^{-1}}$, where the dimension meter refers to the length of the cylinder. At steady state conditions there is no accumulated heat in the system, so the net heat transported out of the control volume must equal the heat flux from the cylinder to the fluid. The heat flux at any given point is given as

$$\mathrm{J}_q = \mathrm{u}h\rho - k\nabla T \tag{3.3}$$

where

$$h = \int_{T_{ref}}^{T} \hat{C}_p dT \tag{3.4}$$

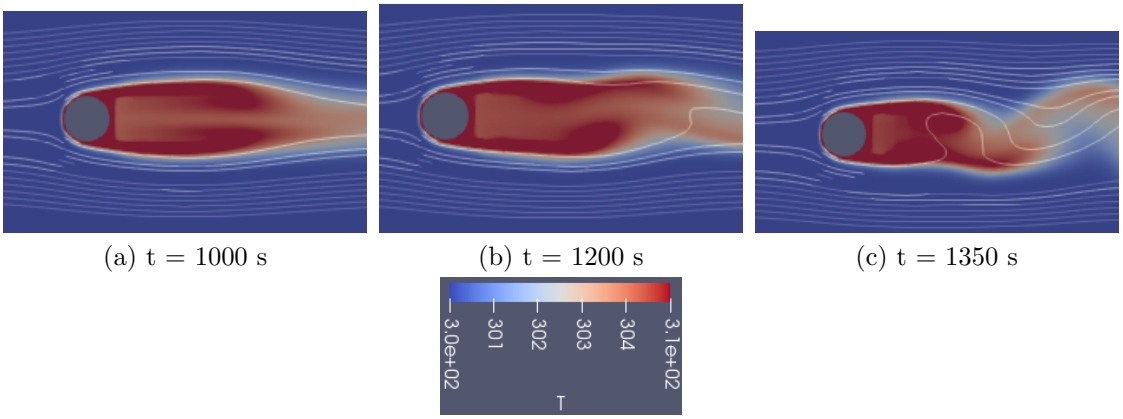

(a) t = 1000 s (b) t = 1200 s (c) t = 1350 s

Figure 3.7: Streamlines and temperature at different times, using water with an inlet velocity $0.005\,\mathrm{m\,s^{-1}}$ as working fluid.

is the specific enthalpy of the fluid at that point, with $\hat{C}_p$ the specific heat capacity. ρ is the fluid density, u is the velocity and k is the thermal conductivity. Assuming that convection dominates heat transfer near the outlet simplifies the equation to

$$\mathrm{J}_q = \mathrm{u}h\rho \tag{3.5}$$

This assumption was tested for the case of water with an inlet velocity of $0.005\,\mathrm{m\,s^{-1}}$, which is the case in which conduction is likely to be most prominent. The temperature profile was extracted along the vertical lines at $x = 0.99\,\mathrm{m}$ and $x = 1\,\mathrm{m}$ to approximate the temperature gradient in the x-direction at the outlet. As shown in Figure 3.8, conductive heat transfer through the outlet is in the order of $1\,\mathrm{W\,m^{-1}}$, about four orders of magnitude smaller than the convective heat transfer shown in Figure 3.9, meaning the the assumption holds.

Setting the reference temperature equal to the inlet temperature, $T_{ref} = 300\,\mathrm{K}$ ensures that the heat flux into the system is zero. Assuming constant heat capacity over the relevant temperature interval results in the expression

$$\mathrm{J}_q = \mathrm{u}\hat{C}_p\rho(T - T_{ref}). \tag{3.6}$$

When calculating the heat flux out of the control volume only the x-component of the heat flux is of interest, this can then be integrated over the outlet giving the expression

$$\dot{q} = \int_{Outlet} u\hat{C}_p\rho(T - T_{ref})dA. \tag{3.7}$$

This calculation has been implemented numerically in python, using ParaView's *Plot over line* functionality to extract the temperature, velocity and density at the outlet. The result is displayed in Figure 3.9. As one would expect, the heat transfer from the cylinder to the fluid increases with increasing inlet velocity, due to reduction of the thermal boundary layer thickness.

At the same time, the average outlet temperature decreases with increasing inlet velocity, this can be attributed to the fact that each fluid element spends less time in the vicinity

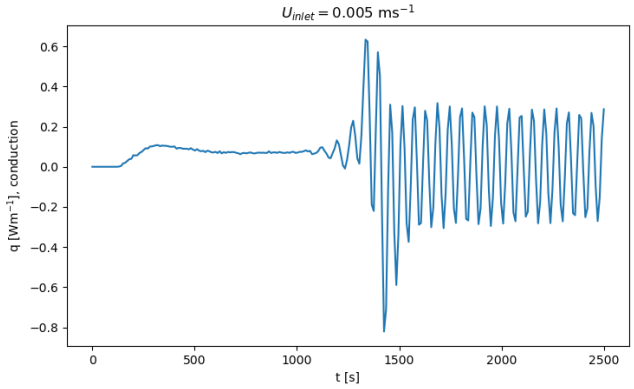

Figure 3.8: Computed conductive heat flux through the outlet as a function of time, using water as working fluid with an inlet velocity $0.005\,\mathrm{m\,s^{-1}}$.

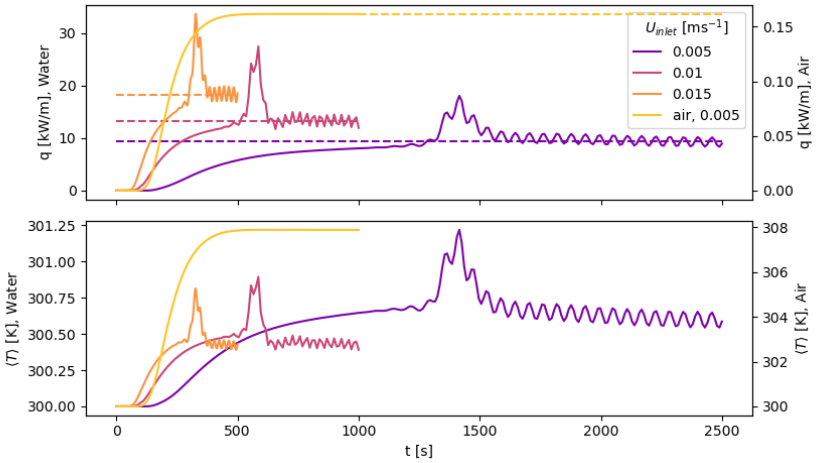

Figure 3.9: Heat flux through the outlet and average outlet temperature as a function of time for different inlet velocities, water is used as working fluid except where otherwise indicated. Heat flux is reported per unit cylinder length.

of the heated cylinder, thereby not being heated as much. The heat flux still increases due to the increase in mass flow, and the reduction in the thermal boundary layer thickness facilitating more efficient heat transfer. The average temperature of air at the outlet is far higher than that of water, this can be attributed to the far lower heat capacity of air.

The expected, analytical heat transfer from the cylinder to the fluid, per unit cylinder length can be computed as

$$\dot{q} = hA(T_s - T_\infty) \tag{3.8}$$

Where $A = 2\pi r$ is the circumference of the cylinder, T_s is the surface temperature of the cylinder, T_∞ is the inlet temperature and

$$h = \frac{\mathrm{Nu}k}{d} \tag{3.9}$$

is the heat transfer coefficient, with

$$\mathrm{Nu} = 0.3 \left(\frac{0.62 \mathrm{Re}^{\frac{1}{2}} \mathrm{Pr}^{\frac{1}{3}}}{1 + (0.4 \mathrm{Pr}^{\frac{2}{3}})^{\frac{1}{4}}} \right) \left(1 + \left(\frac{\mathrm{Re}}{282000} \right)^{\frac{5}{8}} \right)^{\frac{4}{5}}, \tag{3.10}$$

from the Churchill-Bernstein equation,[3] and

$$k = \frac{C_p \mu}{\mathrm{Pr}}. \tag{3.11}$$

A comparison between the computed analytical values and the numerical values from the simulation is shown in Table 3.2. It is immediately clear that there is a discrepancy between the analytical and simulated heat fluxes on the order of 40 % when using water as the working fluid, and that the discrepancy increases with increasing inlet velocity. When using air as the working fluid the discrepancy increases further, to about 75 %.

Table 3.2: Analytical and simulated heat fluxes, reported per unit length of cylinder. *Using air as working fluid.

Inlet Velocity $[\mathrm{m\,s^{-1}}]$	Analytical heat flux $[\mathrm{kW\,m^{-1}}]$	Simulated heat flux $[\mathrm{kW\,m^{-1}}]$	Discrepancy $[\frac{\dot{q}_{\mathrm{analytical}}}{\dot{q}_{\mathrm{simulated}}}]$
0.005	5.84	9.16	0.638
0.01	8.28	13.20	0.627
0.015	10.19	17.88	0.57
0.005*	0.039	0.162	0.241

4 Rising bubbles

An air bubble rising in water from 20 cm below the surface was studied. The effect of varying the bubble diameter and the interfacial tension was investigated. The dimensions of the simulated box were scaled with the bubble diameter to keep the required mesh resolution without drastically increasing the number of mesh cells. In cases 1, 3 and 4 a 0.2m x 0.4m box with air in the upper 10 cm and no slip boundary conditions on all walls was used. In case 2 and 2a a 0.1m x 0.3m box with air in the upper 5 cm and no-slip boundary conditions on all walls was used. Meshes and required computation times are reported in Table 4.1. Note that while the results regarding terminal velocity and bubble shape acquired from simulation case 2a are similar to those acquired from case 2, the latter was run to confirm that the resolution used was indeed high enough. Due to the high computational time, cases 1, 3 and 4 were run with a lower resolution than case 2.

The InterFOAM solver was used, with two inner correctors, 10^{-4} residuals, an implicit Euler time discretisation scheme, a second order Gaussian integration gradient discretisation scheme and a linear interpolation scheme. For the case 3 the effect of using only one inner corrector was investigated. The number of correctors determines the number of times the pressure is computed within each time step.[1,4] In effect, the time step for pressure calculations is reduced by increasing the number of correctors, making it possible to have a stable simulation with longer time steps.

Table 4.1: Computation times for simulations run in section 4. Boundary layer mesh is reported as (Number of layers/expansion factor/initial layer thickness). A boundary layer mesh was only used for the cylinder. *Using only one inner corrector.

Case nr.	Mesh [cells]	Bubble radius [cm]	BL Mesh	Simulated time [s]	Clock time [s]
1	100x200	1	5/1.25/0.2	1.5	554
2	150x250	0.5	2/1.25/0.2	1.5	8660
2a	100x150	0.5	2/1.25/0.2	1.5	392
3	100x200	1	5/1.25/0.2	1.5	722
4*	100x200	1	5/1.25/0.2	1.5	844

4.1 Terminal velocity

The terminal velocity of the bubble was estimated for cases 1-3 shown in Table 4.2. The bubble remained intact until it breached the surface in all cases. The bubble positions as a function of time, shown in Figure 4.1 were approximated by extracting the mass fraction of air α_{air} along a line from the bottom of the geometry to the surface of the water using the *Plot over line* functionality in ParaView. Then the position of the bubble at any given time was approximated as

$$\bar{y}_{\text{bubble}} = \frac{\int_{\text{Bottom}}^{\text{Surface}} y\alpha_{\text{air}} dy}{\int_{\text{Bottom}}^{\text{Surface}} \alpha_{\text{air}} dy}. \tag{4.1}$$

In other words, the center of mass of the bubble along the central vertical line through the geometry. The velocity was then calculated by numerical differentiation to produce the velocity profiles displayed in Figure 4.1. Given that the bubble does not change shape significantly, the position calculated from equation (4.1) will move with the same velocity as the true center of mass of the bubble.

Table 4.2: Bubble conditions investigated in section 4. *Using only one inner corrector.

Case nr.	Bubble radius [cm]	Interfacial tension [N m^{-1}]	Terminal velocity [m s^{-1}]	log(Mo)	Eo
1	1	0.07	0.28	-11.9	1400
2	0.5	0.07	0.22	-11.9	350
3	1	0.35	0.33	-13.8	280
4*	1	0.35	0.33	-13.8	280

4.2 Bubble shape

The development of the bubble shape with time in the three cases investigated is displayed in Figure 4.2. The shapes at 0.45 s is representative of the shape the bubbles had until breaching the surface. Comparing these to the diagram presented by Clift & Grace, [5] shows that while the bubbles in case 1 and 2 are in agreement with the diagram, developing spherical cap shaped bubbles, the bubble in case 3 is not unarguably in agreement.

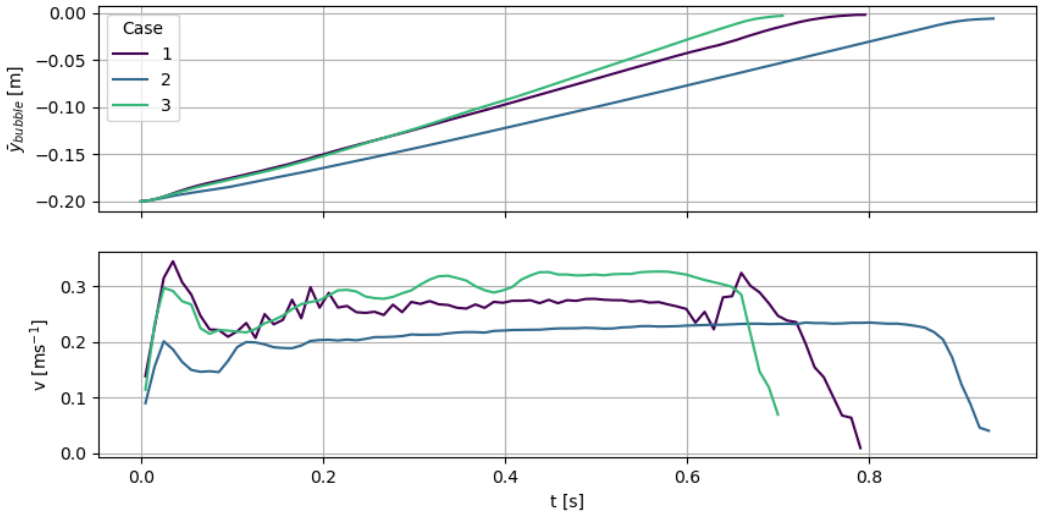

Figure 4.1: Position and velocity of bubble as a function of time in cases 1-3 described in Table 4.2.

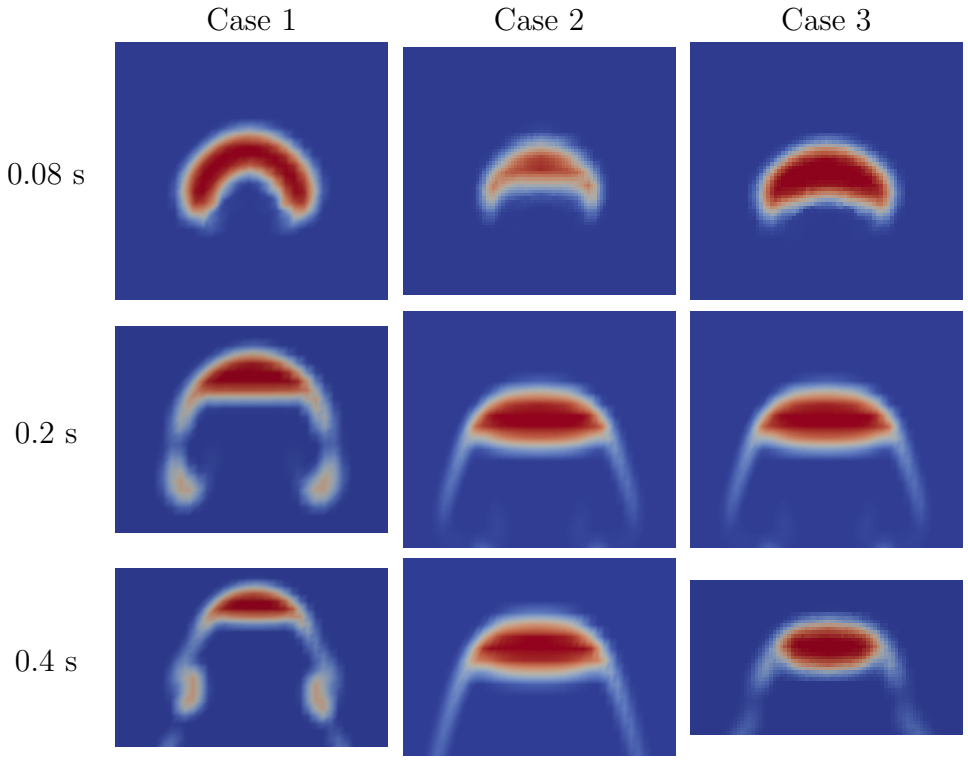

Figure 4.2: Development of bubble shape with time for cases 1-3, described in Table 4.2.

According to the diagram by Clift & Grace this bubble should also develop a spherical capped shape, but is ellipsoidal during most of its journey towards the surface. However, the bubble has a spherical cap shape until it begins "shedding" air that forms smaller bubbles in its wake. As the bubble loses air its Eotvos number is reduced. However, due to the high Morton number a significant reduction in the Eotvos number places the

bubble outside the defined area in the diagram.

Another interesting aspect is the shape of the secondary bubbles formed in the wake of the bubble in case 1, seen clearly at 0.2 s and 0.4 s in Figure 4.2. These necessarily have the same Morton number as the main bubble, but a far lower Eotvos number. As seen from the figure, these have a wobbling shape, in good agreement with the diagram by Clift & Grace.

4.2.1 Changing numerical settings

Changing the number of correctors resulted in the bubble falling apart in the first few time steps, before reforming as shown in Figure 4.3. As the bubble reforms it does so asymmetrically, leading to a tilt. This initial tilt leads to a rocking motion until the bubble breaches the surface at an angle. It is clear from Figure 4.4 that correcting the pressure only once within each time step leads to a far too high pressure inside the bubble at the initial time step. After a few time steps, the computed pressure is in line with that predicted when using two correctors, but the instability caused in the first time step propagates throughout the simulation.

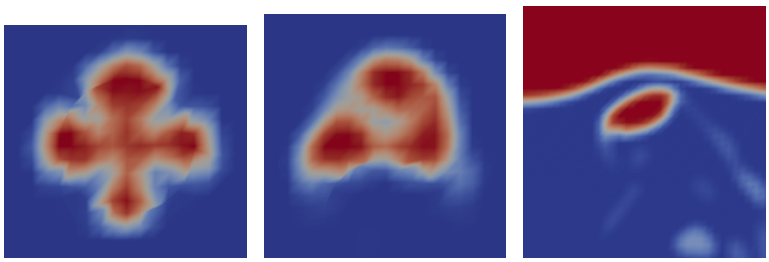

(a) t = 0.02 s (b) t = 0.08 s (c) t = 0.69 s

Figure 4.3: Development of bubble shape with time in case 4.

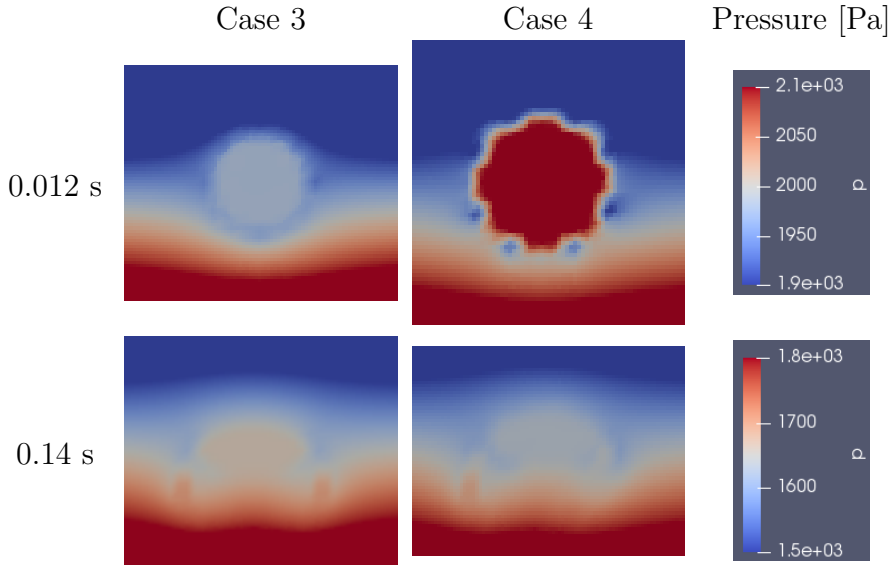

Figure 4.4: Development of pressure with time in cases 3 and 4.

5 Discussion

Regarding the mesh, it is clear that the computational requirement is higher for a transient simulation than for a steady state simulation with the same number of cells, and that a multiphase simulation requires more computational time than a single phase system with heat transfer. In the case of heat transfer presented in section 3.5 it was clear that the results depend heavily on the resolution of the mesh, especially the resolution in the vicinity of the boundary layer.

Changing the gradient discretisation scheme clearly effected the computed wall shear stress in section 2. This was not unexpected, as the wall shear stress is directly dependent on the velocity gradient. However, it was not expected that the change would be by a factor of 5 when a mesh convergence study had already been preformed. As the fourth order least squares interpolation scheme uses both gradients and values of neighbouring cells for interpolation, it is likely more precise than the second order Gaussian interpolation scheme.

It is clear from the observations made in section 4 that using a sufficiently high number of internal correctors can be critical if a physically sound solution is to be acquired. Especially in a multiphase system with essentially unphysical initial conditions (i.e. a stationary, circular bubble of air submerged in water), in this case the primary function of the correctors was to "consolidate" the pressure inside the bubble in the first time step.

References

[1] openfoam.com, "Openfoam documentation." https://www.openfoam.com/documentation/.

[2] M. Nome, "Tma4125 matematikk 4n, lecture notes." https://wiki.math.ntnu.no/tma4125/2019v/start, 2019.

[3] K. Manohar and K. Ramroop, "A comparison of correlations for heat transfer from inclined pipes," *International journal of Engineering*, vol. 4, 2010.

[4] simscale.com, "Cfd pimple algorithm." https://www.simscale.com/forum/t/cfd-pimple-algorithm/81418.

[5] R. Clift, J. Grace, and M. Weber, *Bubbles, Drops, and Particles*. Dover Publications, 01 1978.

A Mesh convergence computation times

A.1 Flow in a cavity

The computation times for the mesh convergence study displayed in Figure 2.2 are shown in Table A.1.

Table A.1: Computation times for mesh convergence study described in section 2.1.

Mesh [cells]	Time [s]	F_y [N]	Mesh [cells]	Time [s]	F_y [N]
15x15	2	1.1391e-09	135x135	54	-4.768e-10
30x30	3	4.532e-10	145x145	66	-4.745e-10
50x50	7	-3.658e-10	155x155	79	-5.07e-10
75x75	13	-2.175e-10	165x165	99	-5.038e-10
85x85	15	-1.208e-10	175x175	123	-5.35e-10
95x95	18	-3.896e-10	185x185	157	-5.304e-10
100x100	19	-3.857e-10	195x195	192	-5.523e-10
105x105	23	-3.959e-10	210x210	252	-5.501e-10
115x115	31	-4.355e-10	250x250	460	-5.667e-10
125x125	45	-4.414e-10			

A.2 Flow around a heated cylinder

Table A.2: Computation times in mesh convergence study for flow around a heated cylinder. Boundary layer meshes are reported as (number of layers/expansion factor/first layer thickness). [1]Using a refined mesh with two levels of refinement extending 5 cm away from the cylinder.

Mesh [cells]	BL Mesh	Heat flux [kW m^{-1}]	Time [s]	Mesh [cells]	BL Mesh	Heat flux [kW m^{-1}]	Time [s]
30x30	5/1.25/0.2	10.8	42	120x120	5/1.25/0.2	13.99	226
50x50	5/1.25/0.2	13.6	67	130x130	5/1.25/0.2	14.01	237
70x70	5/1.25/0.2	15.1	103	100x100	10/1.1/0.2	14.1	238
80x80	5/1.25/0.2	14.9	117	100x100	15/1.1/0.1	12.9	423
90x90	5/1.25/0.2	15.7	134	100x100	15/1.2/0.05	12.5	372
100x100	5/1.25/0.2	14.0	158	100x100	3/1.25/0.5[1]	13.3	492